High-Performance Electrodes for a Hybrid Supercapacitor Derived from a Metal-Organic Framework/Graphene Composite

Yang Jiao,[†] Chong Qu,^{‡,§} Bote Zhao,[‡] Zibin Liang,[§] Huibin Chang,[‡] Satish Kumar,[‡] Ruqiang Zou,^{*,§} Meilin Liu,^{*,‡} and Krista S. Walton^{*,†}

Supporting Information

ABSTRACT: Metal-organic frameworks (MOFs) hold great potential in the development of electrode materials for nextgeneration supercapacitors because of their versatile porous architectures. Here we report our finding in synthesis and characterization of electrode materials derived from a pillared MOF, Ni₂(ADC)₂(DABCO) for a high-performance hybrid supercapacitor, where ADC represents 9,10-anthracenedicarboxylate and DABCO corresponds to 1,4-diazabicyclo [2.2.2] octane. The positive electrode is derived from a single MOF and graphene oxide (GO) composite, consisting of a highly functionalized nickel hydroxide coupled with graphene, ADC, and DABCO groups. A hierarchically porous nitrogen-rich carbon, derived from the same MOF/GO



composite, is used as the negative electrode. The resulting hybrid supercapacitor demonstrates high energy and power density (59 and 48 Wh kg⁻¹ at 0.9 and 15.5 kW kg⁻¹, respectively), good rate capability (19% capacity loss from 1 to 20 Å g⁻¹ and exceptional cycling stability (95% capacity retention over 10000 cycles at 20 A g-1). These findings imply that the combination of pillared MOFs and rGO significantly enhances the electrochemical performance of the resulting electrode materials. In addition, this study also provides a new material preparation strategy (MOFs-rGO-derived materials) for synthesis of high-performance electrode materials for other energy storage devices.

KEYWORDS: supercapacitors, reduced graphene oxide, MOF derivatives, hydroxides, porous carbon

■ INTRODUCTION

The development of advanced materials with excellent electrochemical properties is critical to meet the growing demand of efficient and clean energy sources. Supercapacitors serve as the advanced power sources for portable devices and electric vehicles^{1,2} due to their high power density, rapid charging rate, and long cycling life. 3-5 As a traditional supercapacitor, electrical double-layer capacitors (EDLCs) (e.g., porous carbon) have the potential to be widely used in industrial operations and systems. However, the relatively low energy density of EDLCs restricts their broad applicability.⁶ Hybrid supercapacitors, assembled from a battery-type electrode (e.g., transition metal oxide or hydroxide, especially Ni-based materials) and a capacitive electrode (e.g., porous carbon),^{8,9} have excellent potential to deliver higher energy density than EDLCs because of their broader range of operating voltages and higher capacitance.¹⁰

Among various transition-metal-based candidates for battery-type electrode in supercapacitors, Ni(OH)₂ has received considerable attention due to its high theoretical

capacity.11 Extensive works have been done on the optimization of morphology and porous structure of Ni- $(OH)_{2i}^{12}$ resulting in attractive specific capacity. However, its relatively low cycling stability still limits its widespread use. For example, α -Ni(OH)₂ is often reported to have poor cycling performance, due largely to structural collapse and loss of intercalated crystalline water during the charge-discharge cycling. 11,13 Many efforts have been devoted to improving the structural stability of Ni(OH)₂. For instance, Jing et al. 14 developed an electrochemical altering voltage approach to synthesizing mixed-metal Ni-Co hydroxide. With the incorporation of Co ions, the resulting electrode showed only 8.8% capacity loss after 10000 cycles at the power density of 2.25 kW kg⁻¹. Additionally, a ternary transition mixed-metal hydroxide (Ni-Co-Fe) with a homogeneous distribution was prepared through an idiographic electrochemical method,

Received: April 4, 2019 Accepted: June 5, 2019 Published: June 5, 2019



[†]School of Chemical and Biomolecular Engineering and [‡]School of Materials Science and Engineering, Georgia Institute of Technology, Atlanta, Georgia 30332, United States

[§]Beijing Key Laboratory for Theory and Technology of Advanced Battery Materials, Department of Materials Science and Engineering, College of Engineering, Peking University, Beijing 100871, China

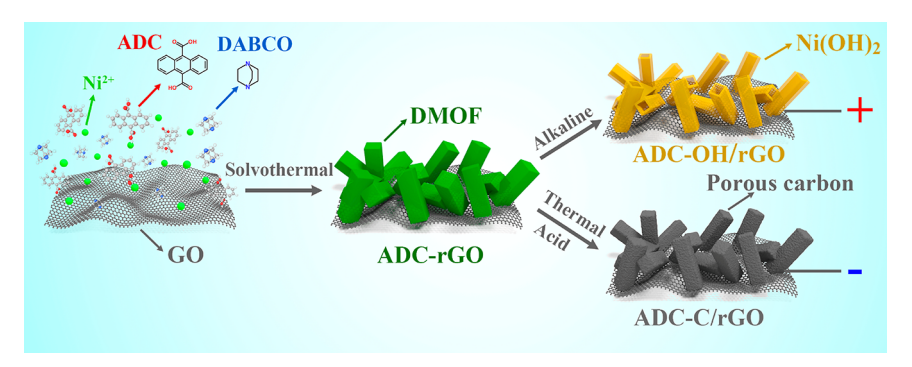


Figure 1. Synthesis procedures for ADC-rGO, ADC-OH/rGO, and ADC-C/rGO.

exhibiting a significantly enhanced cycling stability (4% loss after 20000 cycles at a current density of 34.7 A g⁻¹) in comparison to the binary Ni-Co hydroxide (19% decrease after 20000 cycles). 15 Similarly, Chen et al. reported that the cycling stability of Ni-Co hydroxide was greatly enhanced by its interlayered metaborate groups, which served as pillars to support the layered structures and thus increase the structural stability.¹⁶ The strategy of foreign species incorporation is an effective approach for developing advanced electrodes with excellent cycling stability. However, these as-prepared hydroxides usually have low surface areas, and the synthesis procedures are not always energy efficient. It is imperative to develop a facile approach to the synthesis of highly porous and stable nickel hydroxides.

Metal—organic frameworks (MOFs) are an important subset of crystalline, nanoporous materials, consisting of metalcontaining centers and organic linkers. Compared to traditional porous materials, MOFs exhibit exceptional porosity, ordered porous structure, and diverse functional groups. Because of these interesting features, MOFs have been considered as promising precursors for preparing highperformance electrodes in supercapacitors. 18,19 He et al. reported a facile synthesis of porous Ni-Co hydroxide with high specific capacitance from a MOF template, which was developed based on the mixed-metal strategy. However, the as-prepared hydroxide retained only 73% of its initial capacitance after 10000 cycles.²² This poor cycling stability is due mainly to the rapid loss of the low surface areas and the unstable layered structures during electrochemical cycling. Using mixed-metal MOF-74 as starting materials, we successfully synthesized functionalized Ni-Co hydroxide electrode with enhanced cycling performance (9.9% capacity loss after 5000 cycles at a current density of 20 A g⁻¹) by a simple hydrothermal procedure.²³ This improved cycling stability was ascribed to the synergistic effect of high surface area (299 m² g⁻¹) with hierarchically porous nature and interlayered functional groups (hydroxyl and carboxyl), which were inherited from the MOF precursor.

Some previous works have already shown the potential of MOF-derived materials for developing positive electrodes with remarkable electrochemical performance.²⁴ However, little has been reported for preparation of both positive and negative electrodes from a single MOF precursor. Salunkhe et al. successfully synthesized both positive and negative electrodes from ZIF-67 by altering the thermal treatment conditions.² However, because of the low surface area and poor electronic conductivity, the observed electrochemical performances of these positive (Co₃O₄) and negative (nanoporous carbon) electrodes were not comparable to other derivatives from

MOFs. 19 It is well-known that the electronic conductivity can be significantly enhanced when electrode materials are incorporated with conductive materials such as reduced graphene oxide (graphene) and carbon fiber paper. 10,26 Therefore, a MOF incorporated with conductive additives may represent a promising precursor for high-performance positive and negative electrodes.

In this work, we report the synthesis of a composite composed of a nickel-based pillared MOF (DMOF-ADC)²⁵ and rGO, denoted as ADC-rGO, through a facile solvothermal reaction. We further synthesize both positive electrode (ADCrGO-derived Ni(OH)2, denoted as ADC-OH/rGO) and negative electrode (ADC-rGO-derived carbon, denoted as ADC-C/rGO) materials from a single ADC-rGO composite by choosing appropriate treatments (Figure 1). A microrod morphology with and without inner cavity was observed in both ADC-OH/rGO and ADC-C/rGO by scanning electron microscopy (SEM) and transmission electron microscopy (TEM). The presence of functional species within electrodes was confirmed by X-ray photoelectron spectroscopy (XPS), Raman spectroscopy, and Fourier transform infrared spectroscopy (FTIR) studies. These features were found to foster high performance and cycling stability in both positive and negative electrodes. Additionally, the introduction of rGO has also proven to be beneficial for improving the rate capability (608 and 505 C g⁻¹ at current densities of 1 and 10 A g⁻¹) of the positive electrode ADC-OH/rGO in a three-electrode configuration. Furthermore, a hybrid device was also assembled by using ADC-OH/rGO as the positive electrode and ADC-C/rGO as the negative electrode. The assembled hybrid supercapacitor exhibited superior rate capability (81% capacitance retention varying from 1 to 20 A g⁻¹) and excellent cycling stability (5% loss after 10000 cycles at a current density of 20 A g⁻¹). This study also provides a new material preparation strategy for developing high performance energy storage devices.

EXPERIMENTAL SECTION

Chemicals. All chemicals were used as received without any further purification: Ni(NO₃)₂·6H₂O₂, 9,10-anthracenedicarboxylic acid (H2ADC), NaNO3, KMnO4, KOH, and H2O2 from Sigma-Aldrich, 1,4-diazabicyclo [2.2.2] octane (DABCO) from Acros Organics, N,N-dimethylformamide (DMF), sulfuric acid (H2SO4), and hydrochloric acid (HCl) from VWR, and graphite flake 230U from

Synthesis of Graphene Oxide (GO). The GO was prepared by using a modified Hummers method.³⁰ Typically, graphite flake (1 g, 230U from Asbury) and NaNO₃ (1 g) were mixed with concentrated H₂SO₄ (100 mL) in an ice bath. KMnO₄ (6 g) was added into the mixture while keeping the temperature below 20 °C. The mixture was first stirred in the ice bath for 2 h and in the water bath at 35 °C for another 0.5 h. A 46 mL aliquot of water (70 °C) was added into the mixture. To stop the reaction, 140 mL of water (70 °C) was added in the mixture and followed by 20 mL of H_2O_2 (30 wt %). The mixture was filtrated and washed with abundant water to remove the unreacted species. The obtained GO was dried overnight at 55 °C for further use.

Synthesis of Positive Electrode Material (ADC-OH/rGO). First, the ADC-rGO composite was synthesized by a one-pot solvothermal reaction modified from the literature.²⁹ 80 mg of GO was exfoliated in 40 mL of DMF for 6 h under bath sonication. 1 mmol of Ni(NO₃)₂·6H₂O, 1 mmol of H₂ADC, and 0.5 mmol of DABCO were added in the GO-DMF suspension. After sonication of the suspension for 30 min, the solution was divided into four 20 mL glass vials and placed in a preheated oven at 120 $^{\circ}\text{C}$ for 48 h. The obtained materials were washed repeatedly with DMF and methanol and dried in air for subsequent treatments. ADC-OH/rGO was synthesized by soaking ADC-rGO into 2 M KOH solution for 3 h. The resulting ADC-OH/rGO was washed thoroughly with methanol and dried in air.

Synthesis of Negative Electrode Material (ADC-C/rGO). ADC-C/rGO was synthesized by carbonization of ADC-rGO at 600 $^{\circ}\text{C}$ in N_2 with a heating rate of 1 $^{\circ}\text{C}$ min $^{-1}$ until 500 $^{\circ}\text{C}$ and 2 $^{\circ}\text{C}$ min⁻¹ from 500 to 600 °C. After reaching 600 °C, system was cooled to room temperature with N2 flow. The obtained black powder was washed with concentrated HCl at 80 °C for 4 h to remove nickel residues. The powder was collected by filtration, washed with methanol and deionized water, and dried in air.

Characterization. PXRD patterns of samples were collected on a Panalytical X'Pert PRO Alpha-1 diffraction system with a Cu K α 1 (λ = 1.5418 Å) radiation at room temperature. SEM images of samples were recorded by a Zeiss Ultra60 FE-SEM instrument by using an accelerating voltage of 5 kV. EDS elemental mappings were acquired on the same instrument but with a different accelerating voltage of 10 kV. TEM, high-resolution TEM (HRTEM), and high-angle annular dark-field scanning transmission electron microscopy (HAADF-STEM) images of samples were taken from a FEI Tecnai F30 system. N2 isotherms at 77 K were measured on a Quadrasorb instrument (Quantachrome Instruments). Samples were activated overnight under vacuum at 110 °C, using a Quantachrome FloVac degasser. BET surface areas were determined for the samples by fitting the BET model to the isotherms from 0.05 to 0.3 relative pressure. NLDFT and QSDFT were taken to access the pore size distributions for ADC-OH/rGO and ADC-C/rGO, respectively. XPS measurements were performed on a Thermo K-Alpha XPS instrument (Thermo Fisher Scientific) with a monochromatic Al Ka X-ray source. The spectra were acquired with a step size of 0.1 eV, a spot size of 400 μ m, and a dwell time of 40 ms per increment. Survey spectra were average over three scans, and high-resolution spectra were averaged over at least 15 scans. FTIR spectra from 3000 to 400 cm⁻¹ of samples mixed with dried potassium bromide (KBr) pellets were recorded using an infrared microscope (Spectrum One, PerkinElmer) with a resolution of 4 cm⁻¹. Raman spectra were acquired on samples using a 785 nm laser on a Raman microscope system from HORIBA Scientific.

Electrochemical Measurements. The electrochemical measurements were first performed on a Solartron SI 1286 electrochemical workstation using a three-electrode configuration. For the preparation of ADC-OH/rGO working electrode, ADC-OH/rGO, Super P, and PTFE binder were mixed at a weight ratio of 8:1:1 and then were subsequently rolled with ethanol to form a film with a mass of ~ 3.5 mg cm⁻². The film electrode was compressed between two nickel foams and dried overnight under vacuum at 80 °C. The ADC-C/rGO working electrode was prepared in the same areal mass loading with 90 wt % ADC-rGO-C and 10 wt % PTFE binder. A Pt mesh was used as the counter electrode, and a Ag/AgCl (4 M KCl) electrode was taken as the reference electrode. A 2 M KOH aqueous solution was used as the electrolyte. The cyclic voltammograms were acquired in a potential window of 0-0.5 V at different scan rates. The GCD measurements were performed by varying the potential between 0 and

0.45 V at different current densities. EIS tests were measured from 0.01 to 100 kHz frequency under open-circuit conditions.

The specific capacity Q(C/g) was calculated via eq 1:

$$Q = I\Delta t/m \tag{1}$$

where I (mA) is the discharge current, Δt (s) is the discharge time, and m (mg) is the mass of the active material.

The specific capacitances C (F/g) were calculated via eq 2:

$$C = \frac{2i_m \int V \, dt}{V_i^2 V_f}$$

$$V_i$$
(2)

where $i_m = I/m$ (A g⁻¹) is the current density, I is the current, m is the mass of the active material, $\int V dt$ is the integral current area, V(V) is the potential, and V_i and V_f are the initial and final values of V_i respectively. The cyclic stability was accessed by long-term GCD measurements using a current density of 20 A g-

The electrochemical experiments of hybrid supercapacitor were performed on the same Solartron SI 1286 electrochemical workstation with a two-electrode configuration. The device was fabricated in a split test cell (MTI Corporation) with ADC-OH/rGO as the positive electrode, ADC-C/rGO as the negative electrode, MPF30AC-100 (Nippon Kodoshi Corporation, Kochi, Japan) as the separator, and 2 M KOH solution as the electrolyte. The positive and negative film electrodes were obtained by using the same method as described in the three-electrode configuration. The charges of positive and negative electrodes were calculated based on the cyclic voltammograms obtained from three-electrode configuration by using eq 3:

$$q = \int im \, dV/v \tag{3}$$

where q is the charge, m is the mass of the active material, and $\int i \, dV/$ ν is the integral area from cyclic voltammograms.

To make the charge balance $(q^+=q^-)$, the mass ratio of positive electrode to negative electrode (R) was determined via eq 4:

$$R = m^+: m^- = \left(\int \frac{i \, dV}{v}\right)_-: \left(\int \frac{i \, dV}{v}\right)_+ \tag{4}$$

The CV curves were collected with a voltage from 0 to 1.5 V at different scan rates, and the charge-discharge curves were acquired by varying the voltage between 0 and 1.5 V at different current densities. The cyclic performance was evaluated by long-term GCD experiments at a current density of 20 A g⁻¹. In the Ragone plot of the ADC-OH/rGO//ADC-C/rGO device, the energy density E (Wh kg⁻¹) and power density P (kW kg⁻¹) were calculated according to

$$E = I \int V \, dt/3.6(m_{+} + m_{-}) \tag{5}$$

$$P = \frac{E}{\Delta t} \tag{6}$$

where I is the current (mA), V is the voltage (V), t is the discharge time (s), and m_{+} and m_{-} are the mass of positive and negative active materials, respectively.

RESULTS AND DISCUSSION

As illustrated in Figure 1, the ADC-rGO composite was synthesized according to our previous work²⁹ with the addition of 9 wt % rGO. ADC-rGO was subsequently soaked into 2 M KOH solution for 3 h to obtain ADC-OH/rGO. On the other hand, ADC-C/rGO was prepared through thermal and acid (concentrated HCl) treatments. Powder X-ray diffraction (PXRD) was used to determine the crystalline phase in ADC-rGO, ADC-OH/rGO, and ADC-C/rGO. As shown in Figure S1, ADC-rGO has a similar PXRD pattern to that of DMOF-ADC, suggesting that the formation of MOF crystal is

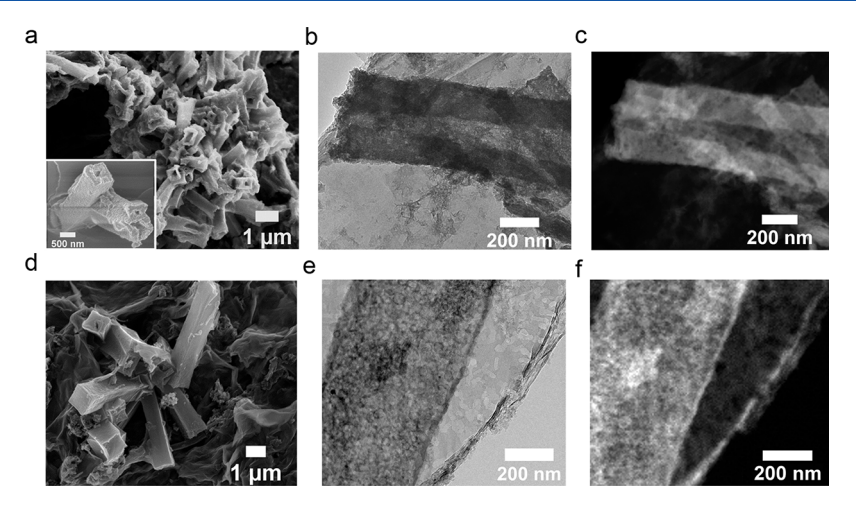


Figure 2. (a-c) SEM, TEM, and HAADF-STEM images of ADC-OH/rGO. (d-f) SEM, TEM, and HAADF-STEM images of ADC-C/rGO.

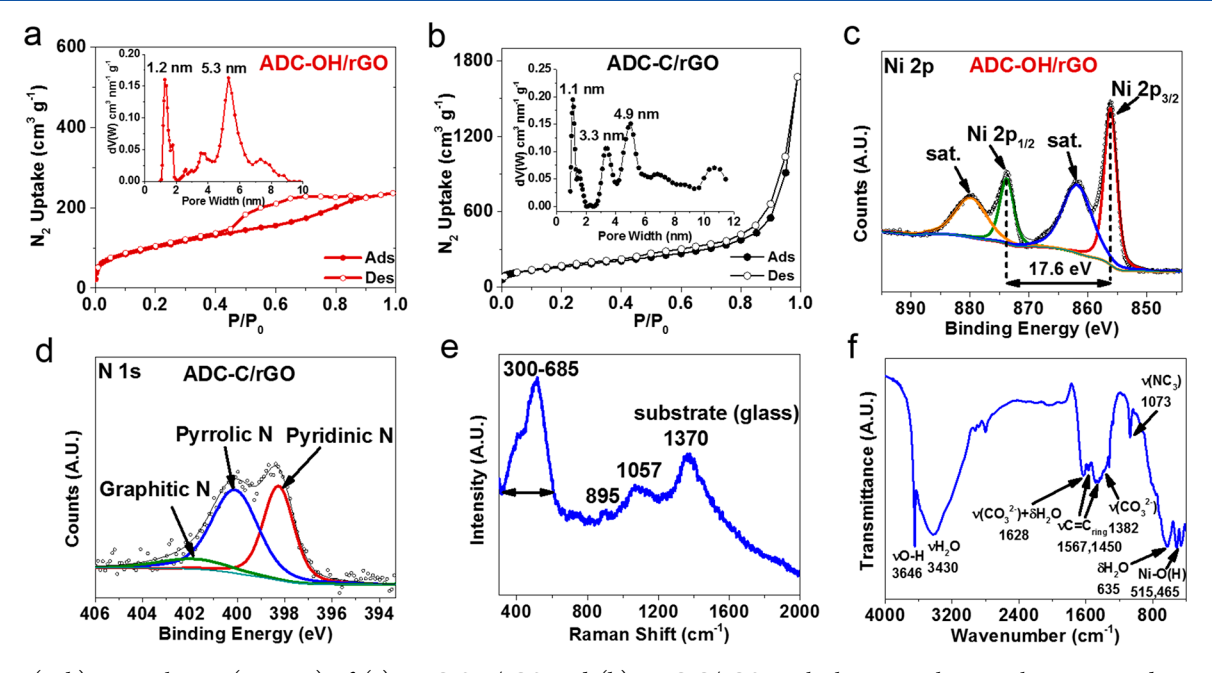


Figure 3. (a, b) N_2 isotherms (at 77 K) of (a) ADC-OH/rGO and (b) ADC-C/rGO, with the insets showing the corresponding pore size distributions (closed symbols: adsorption; open symbols: desorption). (c, d) High-resolution N 1s XPS spectra of (c) ADC-OH/rGO and (d) ADC-C/rGO. (e) Raman and (f) FTIR spectra of ADC-OH.

not prevented upon the incorporation of rGO. In the PXRD pattern of ADC-OH/rGO (Figure S2), the absence of DMOF-ADC peaks and the emergence of β -Ni(OH)₂ (JCPDS No. 14-0117) peaks at 19.3°, 33.1°, 38.5°, 39.1°, 59.0°, and 62.7° illustrate that the transformation from ADC-rGO to ADC-OH/rGO was completed after soaking into 2 M KOH solution for 3 h. Two reflections centered at 26.2° and 44.0° can be seen in the PXRD pattern of ADC-C/rGO (Figure S3), which can be assigned to the (002) and (101) planes of graphitic carbon, respectively. ^{25,31} This observation confirms that ADC-rGO was converted into sp²-bonded graphitic carbon upon thermal treatment.

The morphology of both ADC-OH/rGO and ADC-C/rGO was examined by using SEM and TEM. Compared to the morphology of ADC-rGO (Figure S4), a structural transformation from solid microrods into hollow microrods is observed in ADC-OH/rGO (Figure 2a) upon alkaline treatment. Under strong alkaline solution (2 M KOH), the

metal centers (Ni^{2+}) can dissociate from the organic ligands (ADC and DABCO, see Figure 1) and will also associate with OH⁻ ions, leading to the breakdown of the metal-ligand coordination bonds. As the reaction proceeds, the OH⁻ ions continue to diffuse into and react with the inner part of ADC-rGO; meanwhile, newly formed $Ni(OH)_2$ continuously grows on the preformed $Ni(OH)_2$ layers, resulting in the formation of hollow microrods.

Similar hollow structures were also reported previously when treating MOFs with NaOH or KOH. In line with the SEM observation, TEM images of ADC-OH/rGO (Figure 2b) also confirm the coexistence of hollow microrods and graphene sheets. Additionally, HAADF-STEM was acquired on ADC-OH/rGO (Figure 2c), confirming its hollow structure and porous characteristics. On the contrary, ADC-C/rGO retains a similar morphology to ADC-rGO, which contains abundant hollow microrods with corrugated graphene sheets. As shown in Figure 2d, no obvious inner cavity is observed in these

microrods. A porous carbon rod with few layers of graphene sheets is clearly seen in the TEM image of ADC-C/rGO (Figure 2e). The highly porous nature of ADC-C/rGO was evidenced by the observation of HAADF-STEM (Figure 2f). No bright dots can be seen in ADC-C/rGO, indicating the successful removal of Ni from the structure after reflux with concentrated HCl. HRTEM of ADC-C/rGO in Figure S5 reveals its highly porous carbon nanotube structure and various pore size features.

The electrochemical performance is strongly correlated to the surface area, porosity, and pore size distribution of electrode materials. To explore these properties, N2 physisorption isotherms at 77 K were performed on ADC-OH/rGO and ADC-C/rGO (Figures 3a and 3b). ADC-OH/ rGO displays a high Brunauer-Emmett-Teller (BET) surface area of 309 m² g⁻¹, demonstrating the advantage of MOFs-astemplate synthesis over the conventional methods like electrodeposition or hydrothermal synthesis (typically <100 m^2 g^{-1}). 33-35 The N_2 isotherms of ADC-OH/rGO are classified as type IV with a hysteresis loop starting around P/ $P_0 = 0.4$, implying the formation of mesopores. Nonlocal density functional theory (NLDFT) was used to assess the pore size distributions of ADC-OH/rGO (inset of Figure 3a). The emergence of two sharp peaks at 1.2 and 5.3 nm reveals its hierarchically porous structure with the coexistence of micropores and mesopores. On the other hand, the BET surface area of ADC-C/rGO is 472 m² g⁻¹, which is higher than the nanoporous carbon derived from ZIF-67 (350 m² g^{-1}). The hierarchically porous nature of ADC-C/rGO (inset of Figure 3b) was evidenced by the analysis of pore size distributions using quenched solid state functional theory (QSDFT) method.

XPS was utilized to elucidate the surface characteristics and chemical composition of the as-prepared electrodes. C, N, O, and Ni peaks are all present in the survey spectrum of ADC-OH/rGO (Figure S6a), whereas only C, N, and O peaks are present in the survey spectrum of ADC-C/rGO (Figure S6b), suggesting that nickel residues were removed by acid reflux. In the Ni 2p spectrum of ADC-OH/rGO (Figure 3c), Ni 2p_{3/2} (856.2 eV) and $2p_{1/2}$ (873.8 eV) were detected with two corresponding satellite peaks and a spin-orbit coupling energy of 17.6 eV, which are in agreement with the reported values of Ni(OH)₂. ³⁶ In the high-resolution N 1s spectrum of ADC-OH/rGO (Figure S7), a dominant peak at 400.2 eV can be assigned to the tertiary N bonded to carbon $(N-(C)_3)^{37}$ indicating that some DABCO functional groups are incorporated into the structure. This is expected as ADC-rGO will degrade under alkaline treatment, resulting in the release of DABCO from the MOF framework and the incorporation of DABCO into the as-synthesized nickel hydroxide. Figure S8a presents the high-resolution C 1s spectrum for ADC-OH/ rGO. Detailed deconvolution analysis over the observed peaks shows four components: C-C (284.6 eV), C-O (286.1 eV), C=O (287.9 eV), and C(O)O (289.1 eV). The intensity of the C-O group of the ADC-OH/rGO sample decreased significantly compared to that of GO, indicating that the GO was successfully partially reduced. In the case of ADC-C/rGO, the high-resolution spectrum of C 1s (Figure S8b) can also be assigned to four types of carbon: C-C (284.6 eV), C-O (286.1 eV), C=O (288.1 eV), and C(O)O (289.1 eV). Moreover, the intensities of C-O, C=O, and C(O)O peaks are lower than that of C-C, indicating the GO was reduced by thermal treatment. Contrary to that of ADC-OH/rGO, the

high-resolution N 1s spectrum of ADC-C/rGO (Figure 3d) can be deconvoluted into three species: pyridinic N (398.3 eV), pyrrolic N (400.1 eV), and graphitic N (401.9 eV).³⁸ The formation of these nitrogen species is possibly attributed to the pyrolysis reaction of ADC-rGO precursor during thermal treatment under N₂. Elemental mapping was acquired by energy dispersive spectroscopy (EDS) to reveal the elemental composition and distribution of ADC-OH/rGO and ADC-C/ rGO. As shown in Figure S9, ADC-OH/rGO consists of C, O, N, and Ni with the corresponding atomic percentage of 43.7%, 35.5%, 1.9%, and 18.9%, respectively. On the other hand, ADC-C/rGO (Figure S10) is only composed of C (94.6%), N (3.0%), and O (2.4%) with the absence of Ni element, which is compatible with XPS results. All the detected elements are uniformly distributed throughout ADC-OH/rGO and ADC-C/rGO. Raman spectra for GO, ADC-OH/rGO, and ADCrGO materials are shown in Figure S11. The I_D/I_G ratio of ADC-C/rGO is 1.02, indicating the formation of more defects after pyrolysis.

By use of MOF as the precursor, various functional species can be introduced into the MOF-derived electrode materials. This behavior has been shown to increase the electrochemical performance of the MOF-derived electrodes, 19 particularly the cycling stability.^{23,29} Spectroscopic experiments (FTIR and Raman spectroscopy) are useful to detect the functional groups within the structure. However, the functional groups from graphene sheets, including hydroxyl, carbonyl, and carboxylate groups detected by XPS, may obscure the structural features of ADC-OH/rGO. To avoid this interference from graphene, a similar alkaline treatment was applied on DMOF-ADC to prepare the MOF-derived nickel hydroxide (hereafter noted as ADC-OH) for subsequent analysis. In the Raman spectrum (Figure 3e), the band at 1370 cm⁻¹ is attributed to the glass substrate, which agrees with the blank measurement (Figure S12). A broad band appearing in the range 300–685 cm⁻¹ can be identified as the overlap of Ni-O stretching vibration, resulting from the complicated Ni(OH)₂ structure.^{7,39} Two weak bands with much reduced intensity at 895 and 1057 cm⁻¹ can be assigned to the $v_{25}(vCC)$ mode of ted molecules⁴⁰ and the δ mode of CO_3^{2-} species, 41, respectively. These band features indicate that the prepared MOF derivative ADC-OH is a highly functionalized version of nickel hydroxide with the incorporation of DABCO and CO₃²⁻ species. FTIR analysis (Figure 3f) was conducted to further elucidate the structural characteristics. Two broad bands observed at 3430 and 635 cm⁻¹ correspond to the stretching and bending vibrations of adsorbed water molecules. 42,43 The intense peak at 3646 cm⁻¹ can be identified as the vO-H stretching vibrations, which is the typical characteristic of Ni(OH)₂. ⁴² The bands at 515 and 465 cm⁻¹ are attributed to Ni-OH bending and Ni-O stretching vibrations, further confirming the formation of Ni(OH)₂.⁴⁴ Two small bands centered at 1567 and 1450 cm⁻¹ reflect the C= C_{ring} stretching vibrations of anthracene, ⁴⁵ implying that ADC-OH contains some ADC functional groups after the alkaline treatment. This speculation is further supported by the evidence that two bands were observed at 1382 and 1628 cm⁻¹, which are corresponding to the symmetric and asymmetric stretching vibrations of carboxylate groups, respectively. 46 The band at 1073 cm⁻¹ is attributed to the asymmetric stretching vibration of $N-(C)_3$, ⁴⁷ suggesting that DABCO ligands are also incorporated into the final structure. Considering the FTIR and Raman spectra, it is clear that ADC-OH/rGO is a highly functionalized nickel hydroxide

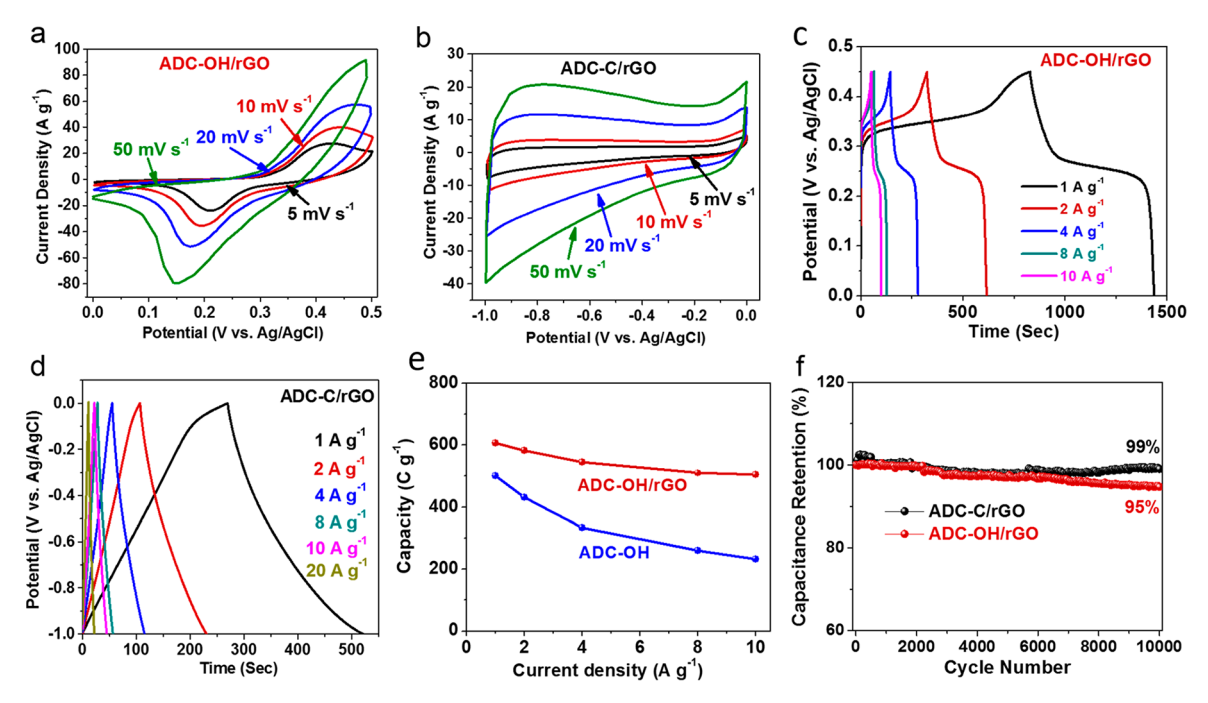


Figure 4. CV curves of (a) ADC-OH/rGO and (b) ADC-C/rGO at different scan rates in 2 M KOH. GCD curves of (c) ADC-OH/rGO and (d) ADC-C/rGO at various current densities. (e) Rate performance of ADC-OH and ADC-OH/rGO. (f) Cycling performance of ADC-OH/rGO and ADC-C/rGO at 20 A g⁻¹.

with incorporation of functional species, including ADC and DABCO groups.

The electrochemical properties of ADC-OH/rGO and ADC-C/rGO were first characterized in three-electrode configurations with 2 M KOH aqueous solution as the electrolyte. Figure 4a presents typical cyclic voltammetric (CV) curves of ADC-OH/rGO measured at various scan rates (5-50 mV s⁻¹) from 0 to 0.5 V (vs Ag/AgCl (KCl)). All the CV curves display a pair of well-defined redox peaks, which are attributed to the reversible reaction of O-H bond breaking/ formation in Ni(OH)₂.^{7,48} Two trends can be observed here: (i) As the scan rate increases, the oxidation peak shifts to the positive direction, whereas the reduction peak moves to a more negative position. This is expected because the internal diffusion resistance of the pseudocapacitive electrode will increase as the scan rate increases. 48,49 (ii) The current increases accordingly as scan rate increases, indicating the good rate capability of ADC-OH/rGO. On the other hand, CV curves of ADC-C/rGO (Figure 4b) were acquired in the potential window of -1.0 to 0 V (vs Ag/AgCl (KCl)), altering scan rates from 10 to 100 mV s⁻¹. In the case of ADC-C/rGO, the curves display similar semirectangular shape, which is the typical behavior of EDLCs. The current of ADC-C/rGO exhibits a positive correlation with the increase of scan rates, implying a good rate capability of ADC-C/rGO. Figure 4c displays the galvanostatic charge-discharge (GCD) curves of ADC-OH/rGO measured at different current densities. The shape of the discharge curves of ADC-OH/rGO indicates an electrochemical redox reaction engaged mechanism which is consistent with the results of CV measurements. The GCD curves (Figure 4d) of ADC-C/rGO collected at various current densities show a triangular fashion, which also corresponds to the electrochemical behavior of EDLCs. The specific capacitances of ADC-C/rGO (Figure S13) were calculated based on the corresponding GCD curves by using eq 2. The specific capacitances are 330, 308, 294, 281, 277, and 269 F g⁻¹

at the corresponding current densities of 1, 2, 4, 8, 10, and 20 A g⁻¹, respectively. When the current density is increased from 1 to 20 A g⁻¹, the specific capacitance retains nearly 81% of the capacitance at 1 A g⁻¹. Such excellent rate capability of ADCrGO is attributed to the incorporation of doped N species⁵⁰ and conductive graphene sheets.¹⁶ Unlike carbon materials, Ni(OH)₂ usually suffers from its limited electronic conductivity, resulting in a relatively poor rate capability.⁵¹ Therefore, it is useful to compare the rate capabilities between ADC-OH and ADC-OH/rGO and understand the effect of graphene sheets on the rate property. To achieve this goal, CV (Figure \$14a) and GCD measurements (Figure \$14b) were also performed on ADC-OH. The specific capacities of ADC-OH/rGO and ADC-OH were calculated from their corresponding GCD curves according to eq 1. The obtained values are plotted in Figure 4e. At the initial current density of 1 A g⁻¹, the specific capacity of ADC-OH (501 C g⁻¹) is lower than that of ADC-OH/rGO (608 C g⁻¹). However, ADC-OH exhibits a poor rate capability with increasing chargedischarge current density from 1 to 10 A g⁻¹. At higher charge-discharge current densities of 8 and 10 A g⁻¹, the specific capacities of ADC-OH retain only 260 and 233 C g⁻¹, corresponding to 52 and 46% of the capacity at 1 A g⁻¹, respectively. On the contrary, with the addition of graphene sheets, ADC-OH/rGO exhibits a much better rate capability than the ADC-OH. At the current densities of 8 and 10 A g⁻¹, the specific capacities remain at 510 and 505 C g⁻¹, which are 84 and 83% of the initial capacity at 1 A g⁻¹. This greatly enhanced rate performance clearly shows the good electronic conductivity of ADC-OH/rGO at high current density region, demonstrating the benefits of incorporating graphene sheets into the electrode. 16,49,52 This promotion of electronic conductivity is further supported by electrochemical impedance spectroscopy (EIS) tests. As shown in Nyquist plots (Figure S15), ADC-OH/rGO has an equivalent series resistance of 0.37 Ω , whereas ADC-OH has a much higher

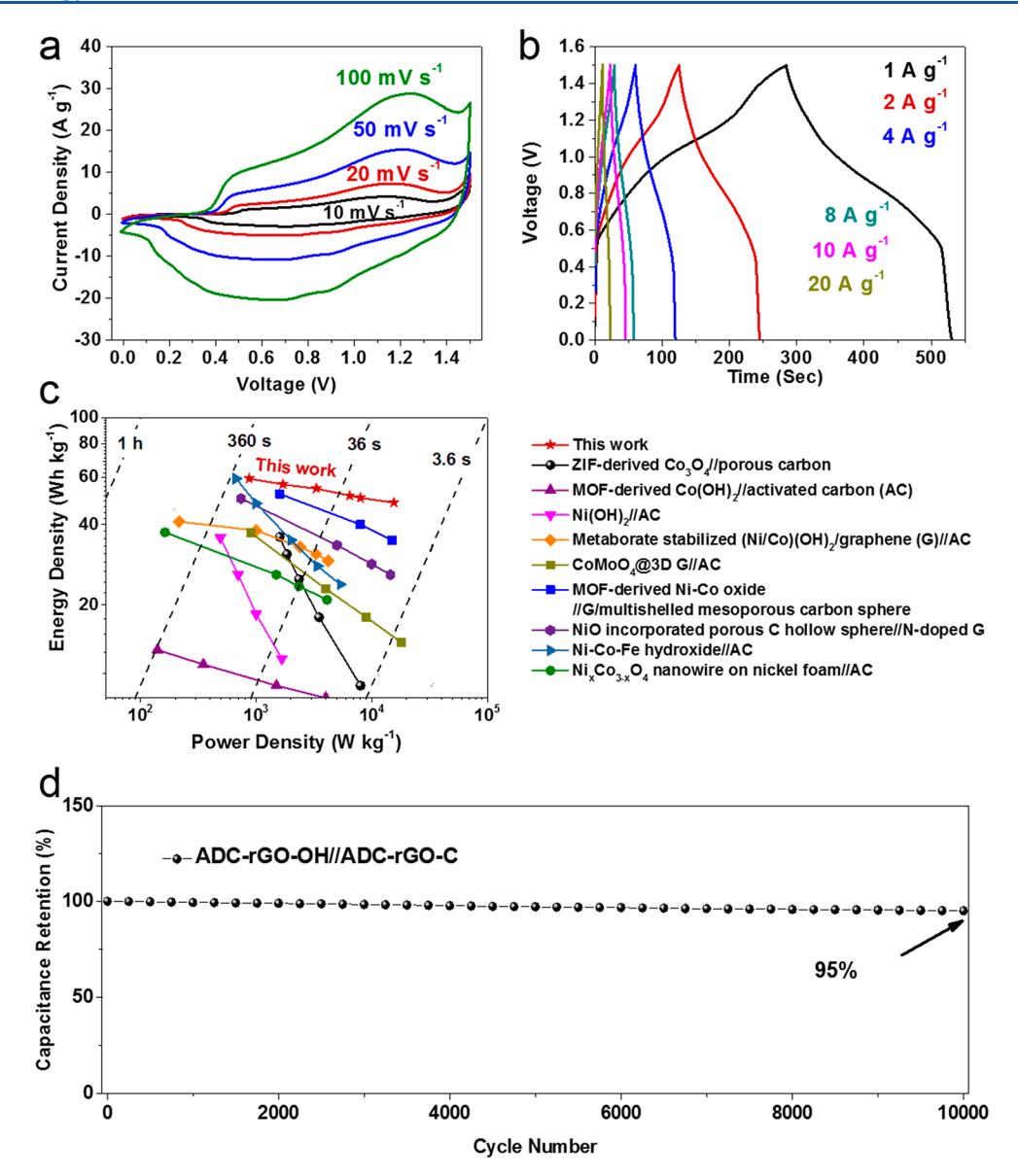


Figure 5. (a) CV curves of ADC-OH/rGO//ADC-C/rGO hybrid supercapacitor device at various scan rates. (b) GCD curves of hybrid device at different current densities. (c) Ragone plot of the ADC-OH/rGO//ADC-C/rGO device compared to those of reported electrodes based on mass of active materials. 11,15,16,25,57-61 (d) Cycling performance of hybrid device at a current density of 20 A g⁻¹.

resistance of 1.02 Ω . Notably, these advanced rate capabilities of ADC-OH/rGO and ADC-C/rGO are comparable to or even better than most of the reported works. 25,53-55 Cycling stability is another parameter of great importance to evaluate the electrochemical performance of electrode. The cycling curves shown in Figure 4f illustrate the change in specific capacity of ADC-OH/rGO and ADC-C/rGO during the longterm galvanostatic measurement (10000 cycles) at a high current density of 20 A g⁻¹. ADC-C/rGO possesses an excellent cycling stability with a retention of 99% after a 10000-cycle test. On the other hand, ADC-OH/rGO has an attractive cycling stability, retaining nearly 95% of its original capacity after 10000 cycles. ADC-OH/rGO delivers much more stable capacity during the long-term run relative to other high-performance Ni(OH)2-graphene or Ni(OH)2-oxide composites. 36,48,56

To further investigate the performance of the as-prepared electrodes under practical conditions, a hybrid supercapacitor (ADC-OH/rGO//ADC-C/rGO) was assembled by using

ADC-OH/rGO and ADC-C/rGO, as the positive and negative electrodes, respectively. To keep the charge balanced, the mass ratio of negative and positive electrode was set to 2.2 according to the corresponding CV curves of ADC-C/rGO and ADC-OH/rGO (eqs 3 and 4). As shown in Figures 5a and 5b, the fabricated hybrid supercapacitor can be operated in a broad potential window of 0-1.5 V. Figure 5a presents the CV curves collected at different scan rates, ranging from 10 to 100 mV s⁻¹ (individual CV curves of positive and negative electrodes are shown in Figure S16a). It is clear that the shape of the obtained CV curves indicates the convolution of two different energy storage characteristics, which agrees with the results of CV studies in the three-electrode system. The shape of the CV curves is retained in a similar fashion as the scan rate increases, indicating the good rate capability of the device. Figure 5b summarizes the corresponding GCD curves of the hybrid supercapacitor acquired at different current densities from 1 to 20 A g⁻¹. An inclined plateau from 1.1 to 0.3 V is observed in the discharge curves, which are compatible with the CV trends.

Figure S16b illustrates the relationship between specific capacities/capacitances of the hybrid supercapacitor and current densities from 1 to 20 A g⁻¹. An outstanding rate performance is achieved such that 81% of the capacitance at 1 A g^{-1} is maintained when the current density is increased to 20 A g⁻¹. This excellent behavior can be attributed to the good rate capabilities of ADC-OH/rGO and ADC-C/rGO electrodes. Figure 5c presents the relationship between the gravimetric energy density and power density (Ragone plot) of the ADC-OH/rGO//ADC-C/rGO device. Based on egs 5 and 6, this device delivers a high energy density of 59 W h ${\rm kg}^{-1}$ at a power density of 872 W kg⁻¹. Moreover, an energy density of 48 W h kg⁻¹ is preserved, as the power density elevates up to 15.5 kW kg⁻¹. Notably, ADC-OH/rGO//ADC-C/rGO displays much higher energy and power densities in comparison to those previously reported devices fabricated by highperformance electrode materials (Figure 5c), including MOF-derived materials, ^{25,57,58} metal hydroxide or oxide materials, 11,15,59 and metal hydroxide or oxide composites embedded with graphene or conductive carbon. 16,60,61 The cycling performance of energy storage device at high chargedischarge rates is always the essential requirement for practical processes.⁶² As shown in Figure 5d, a capacitance retention of 95% is maintained in this hybrid supercapacitor when being tested at a high current density of 20 A g⁻¹ over 10000 cycles. Compared to the reported results, ADC-OH/rGO//ADC-C/ rGO is one of the most stable hybrid/asymmetric supercapacitor devices (Table S1). 15,16,23,57,61,63

Several features may contribute to the excellent electrochemical performance of the ADC-OH/rGO//ADC-C/rGO device: (i) the highly porous nature and micro-mesoporous structure inherited from MOF-rGO template not only improve the contact between electrode and electrolyte during faradaic reaction but also shorten ionic diffusion pathways for electrolyte molecules; (ii) the functional groups (ADC and DABCO species) derived from MOF-rGO precursor might serve as pillars within the structure, resulting in the excellent cycling performance. To be more specific, ADC and DABCO species are anchored within the layered structure of MOFderived nickel hydroxides. During the charge-discharge reaction, the volume expansion or shrinkage of highly functionalized nickel hydroxide was constrained by these functional groups. These functional groups prevent the structural collapse in early cycles. (iii) The doped N species within ADC-C/rGO can function as electrochemically active sites and further increase the capacity. (iv) The electronic conductivities of MOF-derived electrodes are significantly enhanced by the presence of rGO, offering efficient electron transport at fast charge-discharge rates.

CONCLUSION

In summary, we have synthesized a novel MOF-rGO composite containing a nickel-based pillared MOF (DMOF-ADC) and reduced graphene oxide using a simple solvothermal procedure. MOF-rGO was used as the precursor and subsequently converted to both positive (ADC-OH/rGO) and negative (ADC-C/rGO) electrodes by different treatments. Supported by the analysis of N_2 physisorption measurements and pore size distributions, the MOF-rGO-derived electrodes, ADC-OH/rGO and ADC-C/rGO, demonstrate remarkably high surface areas and contain hybrid characteristics of micro- and mesopores. In particular, ADC-OH/rGO is found to be functionalized with multiple

functional groups (ADC and DABCO), as confirmed by XPS, Raman, and FTIR analyses. When tested in a threeelectrode configuration, ADC-OH/rGO and ADC-C/rGO exhibited high performance and cycling stability. Moreover, ADC-OH/rGO exhibited 83% capacity retention as the current density was changed from 1 to 10 A g⁻¹, demonstrating the key role of graphene in increasing the conductivity. A hybrid supercapacitor has been further assembled from a positive ADC-OH/rGO electrode and a negative ADC-C/rGO electrode. With the contributions of both graphene sheets and functional groups, the obtained hybrid supercapacitor exhibits an excellent rate capability (~19% capacity loss as cycling rate is changed from 1 to 20 A g⁻¹) and an exceptional cycling stability (95% capacity retention after 10000 cycles). The present MOF-rGO-derived material preparation strategy is applicable to the development of high-performance electrode materials for other advanced energy storage systems.

ASSOCIATED CONTENT

Supporting Information

The Supporting Information is available free of charge on the ACS Publications website at DOI: 10.1021/acsaem.9b00700.

PXRD patterns, SEM images, XPS spectra, EDX mapping data, Raman spectrum, HR-TEM images, electrochemical rate performance, CV curves, Nyquist plots, and cycling performance comparison with the literature (PDF)

AUTHOR INFORMATION

Corresponding Authors

*(R.Z.) E-mail: rzou@pku.edu.cn.

*(M.L.) E-mail: meilin.liu@mse.gatech.edu.

*(K.S.W.) E-mail: krista.walton@chbe.gatech.edu.

ORCID 🌕

Yang Jiao: 0000-0002-6634-9155 Bote Zhao: 0000-0003-1236-6862 Ruqiang Zou: 0000-0003-0456-4615 Meilin Liu: 0000-0002-6188-2372 Krista S. Walton: 0000-0002-0962-9644

Author Contributions

Y.J., C.Q., and B.Z. contributed equally to this work.

Notes

The authors declare no competing financial interest.

ACKNOWLEDGMENTS

This work was supported by the Center for Understanding and Control of Acid Gas-induced Evolution of Materials for Energy, an Energy Frontier Research Center funded by DOE, Office of Science, BES under Award DESC0012577 (Y.J. and K.S.W.), the US National Science Foundation under award number DMR-1742828, and Guangdong Innovative and Entrepreneurial Research Team Program (No. 2014ZT05N200).

REFERENCES

(1) Lu, X. H.; Yu, M. H.; Wang, G. M.; Tong, Y. X.; Li, Y. Flexible solid-state supercapacitors: design, fabrication and applications. *Energy Environ. Sci.* **2014**, *7* (7), 2160–2181.

(2) Karden, E.; Ploumen, S.; Fricke, B.; Miller, T.; Snyder, K. Energy storage devices for future hybrid electric vehicles. *J. Power Sources* **2007**, *168* (1), 2–11.

- (3) Li, J.; Liu, Z.; Zhang, Q.; Cheng, Y.; Zhao, B.; Dai, S.; Wu, H.-H.; Zhang, K.; Ding, D.; Wu, Y.; Liu, M.; Wang, M.-S. Anion and cation substitution in transition-metal oxides nanosheets for highperformance hybrid supercapacitors. Nano Energy 2019, 57, 22-33.
- (4) Zhang, Q.; Liu, Z.; Zhao, B.; Cheng, Y.; Zhang, L.; Wu, H.-H.; Wang, M.-S.; Dai, S.; Zhang, K.; Ding, D.; Wu, Y.; Liu, M. Design and understanding of dendritic mixed-metal hydroxide nanosheets@Ndoped carbon nanotube array electrode for high-performance asymmetric supercapacitors. Energy Storage Mater. 2019, 16, 632-
- (5) Zhao, B.; Zhang, L.; Zhang, Q.; Chen, D.; Cheng, Y.; Deng, X.; Chen, Y.; Murphy, R.; Xiong, X.; Song, B.; Wong, C.-P.; Wang, M.-S.; Liu, M. Rational Design of Nickel Hydroxide-Based Nanocrystals on Graphene for Ultrafast Energy Storage. Adv. Energy Mater. 2018, 8 (9), 1702247.
- (6) Zhong, C.; Deng, Y. D.; Hu, W. B.; Qiao, J. L.; Zhang, L.; Zhang, J. J. A review of electrolyte materials and compositions for electrochemical supercapacitors. Chem. Soc. Rev. 2015, 44 (21),
- (7) Xiong, X. H.; Ding, D.; Chen, D. C.; Waller, G.; Bu, Y. F.; Wang, Z. X.; Liu, M. L. Three-dimensional ultrathin Ni(OH)(2) nanosheets grown on nickel foam for high-performance supercapacitors. Nano Energy 2015, 11, 154-161.
- (8) Young, C.; Park, T.; Yi, J. W.; Kim, J.; Hossain, M. S. A.; Kaneti, Y. V.; Yamauchi, Y. Advanced Functional Carbons and Their Hybrid Nanoarchitectures towards Supercapacitor Applications. ChemSusChem 2018, 11 (20), 3546-3558.
- (9) Young, C.; Kim, J.; Kaneti, Y. V.; Yamauchi, Y. One-Step Synthetic Strategy of Hybrid Materials from Bimetallic Metal-Organic Frameworks for Supercapacitor Applications. ACS Applied Energy Materials 2018, 1 (5), 2007-2015.
- (10) Zhao, B.; Chen, D.; Xiong, X.; Song, B.; Hu, R.; Zhang, Q.; Rainwater, B. H.; Waller, G. H.; Zhen, D.; Ding, Y.; Chen, Y.; Qu, C.; Dang, D.; Wong, C.-P.; Liu, M. A high-energy, long cycle-life hybrid supercapacitor based on graphene composite electrodes. Energy Storage Mater. 2017, 7, 32-39.
- (11) Li, H. B.; Yu, M. H.; Wang, F. X.; Liu, P.; Liang, Y.; Xiao, J.; Wang, C. X.; Tong, Y. X.; Yang, G. W. Amorphous nickel hydroxide nanospheres with ultrahigh capacitance and energy density as electrochemical pseudocapacitor materials. Nat. Commun. 2013, 4,
- (12) Matsui, K.; Kyotani, T.; Tomita, A. Hydrothermal synthesis of single-crystal Ni(OH)(2) nanorods in a carbon-coated anodic alumina film. Adv. Mater. 2002, 14 (17), 1216-1217.
- (13) Jiang, H.; Zhao, T.; Li, C. Z.; Ma, J. Hierarchical self-assembly of ultrathin nickel hydroxide nanoflakes for high-performance supercapacitors. J. Mater. Chem. 2011, 21 (11), 3818-3823.
- (14) Jing, M. J.; Hou, H. S.; Banks, C. E.; Yang, Y. C.; Zhang, Y.; Ji, X. B. Alternating Voltage Introduced NiCo Double Hydroxide Layered Nanoflakes for an Asymmetric Supercapacitor. ACS Appl. Mater. Interfaces 2015, 7 (41), 22741-22744.
- (15) Li, H. B.; Gao, Y. Q.; Wang, C. X.; Yang, G. W. A Simple Electrochemical Route to Access Amorphous Mixed-Metal Hydroxides for Supercapacitor Electrode Materials. Adv. Energy Mater. 2015, 5, 1401767.
- (16) Chen, Y. Z.; Pang, W. K.; Bai, H. H.; Zhou, T. F.; Liu, Y. N.; Li, S.; Guo, Z. P. Enhanced Structural Stability of Nickel-Cobalt Hydroxide via Intrinsic Pillar Effect of Metaborate for High-Power and Long-Life Supercapacitor Electrodes. Nano Lett. 2017, 17 (1),
- (17) Furukawa, H.; Cordova, K. E.; O'Keeffe, M.; Yaghi, O. M. The Chemistry and Applications of Metal-Organic Frameworks. Science **2013**, *341* (6149), 1230444–1230444.
- (18) Wang, H.; Zhu, Q.-L.; Zou, R.; Xu, Q. Metal-Organic Frameworks for Energy Applications. Chem. 2017, 2 (1), 52-80.
- (19) Zheng, S.; Li, X.; Yan, B.; Hu, Q.; Xu, Y.; Xiao, X.; Xue, H.; Pang, H. Transition-Metal (Fe, Co, Ni) Based Metal-Organic Frameworks for Electrochemical Energy Storage. Adv. Energy Mater. 2017, 7, 1602733.

- (20) Wang, L. J.; Deng, H. X.; Furukawa, H.; Gandara, F.; Cordova, K. E.; Peri, D.; Yaghi, O. M. Synthesis and Characterization of Metal-Organic Framework-74 Containing 2, 4, 6, 8, and 10 Different Metals. Inorg. Chem. 2014, 53 (12), 5881-5883.
- (21) Jiao, Y.; Morelock, C. R.; Burtch, N. C.; Mounfield, W. P.; Hungerford, J. T.; Walton, K. S. Tuning the Kinetic Water Stability and Adsorption Interactions of Mg-MOF-74 by Partial Substitution with Co or Ni. Ind. Eng. Chem. Res. 2015, 54 (49), 12408-12414.
- (22) He, S. H.; Li, Z. P.; Wang, J. Q.; Wen, P.; Gao, J. C.; Ma, L. M.; Yang, Z. G.; Yang, S. R. MOF-derived NixCo1-x(OH)(2) composite microspheres for high-performance supercapacitors. RSC Adv. 2016, 6 (55), 49478-49486.
- (23) Qu, C.; Zhao, B.; Jiao, Y.; Chen, D.; Dai, S.; deglee, B. M.; Chen, Y.; Walton, K. S.; Zou, R.; Liu, M. Functionalized Bimetallic Hydroxides Derived from Metal-Organic Frameworks for High-Performance Hybrid Supercapacitor with Exceptional Cycling Stability. ACS Energy Lett. 2017, 2 (6), 1263-1269.
- (24) Xie, Z. Q.; Xu, W. W.; Cui, X. D.; Wang, Y. Recent Progress in Metal-Organic Frameworks and Their Derived Nanostructures for Energy and Environmental Applications. ChemSusChem 2017, 10 (8), 1645-1663.
- (25) Salunkhe, R. R.; Tang, J.; Kamachi, Y.; Nakato, T.; Kim, J. H.; Yamauchi, Y. Asymmetric Supercapacitors Using 3D Nanoporous Carbon and Cobalt Oxide Electrodes Synthesized from a Single Metal-Organic Framework. ACS Nano 2015, 9 (6), 6288-6296.
- (26) Fan, Z. J.; Yan, J.; Wei, T.; Zhi, L. J.; Ning, G. Q.; Li, T. Y.; Wei, F. Asymmetric Supercapacitors Based on Graphene/MnO2 and Activated Carbon Nanofiber Electrodes with High Power and Energy Density. Adv. Funct. Mater. 2011, 21 (12), 2366-2375.
- (27) Huang, L.; Chen, D. C.; Ding, Y.; Feng, S.; Wang, Z. L.; Liu, M. L. Nickel-Cobalt Hydroxide Nanosheets Coated on NiCo2O4 Nanowires Grown on Carbon Fiber Paper for High-Performance Pseudocapacitors. Nano Lett. 2013, 13 (7), 3135-3139.
- (28) Tao, J. Y.; Liu, N. S.; Ma, W. Z.; Ding, L. W.; Li, L. Y.; Su, J.; Gao, Y. H. Solid-State High Performance Flexible Supercapacitors Based on Polypyrrole-MnO2-Carbon Fiber Hybrid Structure. Sci. Rep. 2013, 3, 2286.
- (29) Qu, C.; Jiao, Y.; Zhao, B.; Chen, D.; Zou, R.; Walton, K. S.; Liu, M. Nickel-based pillared MOFs for high-performance supercapacitors: Design, synthesis and stability study. Nano Energy 2016, 26, 66-73.
- (30) Lian, G.; Tuan, C. C.; Li, L. Y.; Jiao, S. L.; Wang, Q. L.; Moon, K. S.; Cui, D. L.; Wong, C. P. Vertically Aligned and Interconnected Graphene Networks for High Thermal Conductivity of Epoxy Composites with Ultralow Loading. Chem. Mater. 2016, 28 (17),
- (31) Xia, W.; Qu, C.; Liang, Z.; Zhao, B.; Dai, S.; Qiu, B.; Jiao, Y.; Zhang, Q.; Huang, X.; Guo, W.; Dang, D.; Zou, R.; Xia, D.; Xu, Q.; Liu, M. High-Performance Energy Storage and Conversion Materials Derived from a Single Metal-Organic Framework/Graphene Aerogel Composite. Nano Lett. 2017, 17 (5), 2788-2795.
- (32) Zhang, L.; Wu, H. B.; Lou, X. W. Metal-Organic-Frameworks-Derived General Formation of Hollow Structures with High Complexity. J. Am. Chem. Soc. 2013, 135 (29), 10664-10672.
- (33) Gupta, V.; Gupta, S.; Miura, N. Statically deposited nanostructured CoxNi1-x layered double hydroxides as electrode materials for redox-supercapacitors. J. Power Sources 2008, 175 (1), 680 - 685.
- (34) Shao, M. F.; Ning, F. Y.; Zhao, Y. F.; Zhao, J. W.; Wei, M.; Evans, D. G.; Duan, X. Core-Shell Layered Double Hydroxide Microspheres with Tunable Interior Architecture for Supercapacitors. Chem. Mater. 2012, 24 (6), 1192-1197.
- (35) Parveen, N.; Cho, M. H. Self-Assembled 3D Flower-Like Nickel Hydroxide Nanostructures and Their Supercapacitor Applications. Sci. Rep. 2016, 6, 27318.
- (36) Yan, J.; Fan, Z. J.; Sun, W.; Ning, G. Q.; Wei, T.; Zhang, Q.; Zhang, R. F.; Zhi, L. J.; Wei, F. Advanced Asymmetric Supercapacitors Based on Ni(OH)2/Graphene and Porous Graphene Electrodes with High Energy Density. Adv. Funct. Mater. 2012, 22 (12), 2632-2641.

- (37) Ong, W. J.; Tan, L. L.; Chai, S. P.; Yong, S. T. Heterojunction engineering of graphitic carbon nitride (g-C3N4) via Pt loading with improved daylight-induced photocatalytic reduction of carbon dioxide to methane. *Dalton Trans.* **2015**, *44* (3), 1249–1257.
- (38) Wang, X. J.; Zhou, J. W.; Fu, H.; Li, W.; Fan, X. X.; Xin, G. B.; Zheng, J.; Li, X. G. MOF derived catalysts for electrochemical oxygen reduction. *J. Mater. Chem. A* **2014**, 2 (34), 14064–14070.
- (39) Yang, Y.; Li, L.; Ruan, G. D.; Fei, H. L.; Xiang, C. S.; Fan, X. J.; Tour, J. M. Hydrothermally Formed Three-Dimensional Nanoporous Ni(OH)(2) Thin-Film Supercapacitors. *ACS Nano* **2014**, 8 (9), 9622–9628.
- (40) Guzonas, D. A.; Irish, D. E. A Raman and infrared spectroscopic study of triethylenediamine (DABCO) and its protonated forms. *Can. J. Chem.* 1988, 66 (5), 1249–1257.
- (41) Lunsford, J. H.; Yang, X. M.; Haller, K.; Laane, J.; Mestl, G.; Knozinger, H. In situ Raman spectroscopy of peroxide ions on barium/magnesium oxide catalysts. *J. Phys. Chem.* **1993**, *97* (51), 13810–13813.
- (42) Cha, S. M.; Nagaraju, G.; Yu, J. S. Controlled Electrochemical Synthesis of Nickel Hydroxide Nanosheets Grown on Non-woven Cu/PET Fibers: A Robust, Flexible, and Binder-Free Electrode for High-Performance Pseudocapacitors. *J. Phys. Chem. C* **2016**, *120* (33), 18411–18420.
- (43) Yang, S. B.; Wu, X. L.; Chen, C. L.; Dong, H. L.; Hu, W. P.; Wang, X. K. Spherical alpha-Ni(OH)(2) nanoarchitecture grown on graphene as advanced electrochemical pseudocapacitor materials. *Chem. Commun.* **2012**, 48 (22), 2773–2775.
- (44) Xu, P.; Han, X. J.; Zhang, B.; Lv, Z. S.; Liu, X. R. Characterization of an ultrafine beta-nickel hydroxide from supersonic co-precipitation method. *J. Alloys Compd.* **2007**, 436 (1–2), 369–374.
- (45) Mary, Y. S.; Jojo, P. J.; Van Alsenoy, C.; Kaur, M.; Siddegowda, M. S.; Yathirajan, H. S.; Nogueira, H. I. S.; Cruz, S. M. A. Vibrational spectroscopic (FT-IR, FT-Raman, SERS) and quantum chemical calculations of 3-(10,10-dimethyl-anthracen-9-ylidene)-N,N,N-trimethylpropanaminiium chloride (Melitracenium chloride). *Spectrochim. Acta, Part A* **2014**, *120*, 370–380.
- (46) Taibi, M.; Ammar, S.; Jouini, N.; Fievet, F.; Molinie, P.; Drillon, M. Layered nickel hydroxide salts: synthesis, characterization and magnetic behaviour in relation to the basal spacing. *J. Mater. Chem.* **2002**, *12* (11), 3238–3244.
- (47) Tan, K.; Nijem, N.; Canepa, P.; Gong, Q.; Li, J.; Thonhauser, T.; Chabal, Y. J. Stability and Hydrolyzation of Metal Organic Frameworks with Paddle-Wheel SBUs upon Hydration. *Chem. Mater.* **2012**, 24 (16), 3153–3167.
- (48) Ji, J. Y.; Zhang, L. L.; Ji, H. X.; Li, Y.; Zhao, X.; Bai, X.; Fan, X. B.; Zhang, F. B.; Ruoff, R. S. Nanoporous Ni(OH) Thin Film on 3D Ultrathin-Graphite Foam for Asymmetric Supercapacitor. *ACS Nano* **2013**, *7* (7), 6237–6243.
- (49) Wang, H. L.; Casalongue, H. S.; Liang, Y. Y.; Dai, H. J. Ni(OH)(2) Nanoplates Grown on Graphene as Advanced Electrochemical Pseudocapacitor Materials. *J. Am. Chem. Soc.* **2010**, 132 (21), 7472–7477.
- (50) Hulicova-Jurcakova, D.; Seredych, M.; Lu, G. Q.; Bandosz, T. J. Combined Effect of Nitrogen- and Oxygen-Containing Functional Groups of Microporous Activated Carbon on its Electrochemical Performance in Supercapacitors. *Adv. Funct. Mater.* **2009**, *19* (3), 438–447.
- (51) Wang, G. P.; Zhang, L.; Zhang, J. J. A review of electrode materials for electrochemical supercapacitors. *Chem. Soc. Rev.* **2012**, 41 (2), 797–828.
- (52) Cao, X. H.; Zheng, B.; Shi, W. H.; Yang, J.; Fan, Z. X.; Luo, Z. M.; Rui, X. H.; Chen, B.; Yan, Q. Y.; Zhang, H. Reduced Graphene Oxide-Wrapped MoO3 Composites Prepared by Using Metal-Organic Frameworks as Precursor for All-Solid-State Flexible Supercapacitors. *Adv. Mater.* 2015, 27 (32), 4695–4701.
- (53) Salunkhe, R. R.; Kamachi, Y.; Torad, N. L.; Hwang, S. M.; Sun, Z. Q.; Dou, S. X.; Kim, J. H.; Yamauchi, Y. Fabrication of symmetric supercapacitors based on MOF-derived nanoporous carbons. *J. Mater. Chem. A* **2014**, 2 (46), 19848–19854.

- (54) Xiang, Z. H.; Wang, D.; Xue, Y. H.; Dai, L. M.; Chen, J. F.; Cao, D. P. PAF-derived nitrogen-doped 3D Carbon Materials for Efficient Energy Conversion and Storage. *Sci. Rep.* **2015**, *5*, 8307.
- (55) Abushrenta, N.; Wu, X. C.; Wang, J. N.; Liu, J. F.; Sun, X. M. Hierarchical Co-based Porous Layered Double Hydroxide Arrays Derived via Alkali Etching for High-performance Supercapacitors. *Sci. Rep.* **2015**, *5*, 13082.
- (56) Chen, H.; Hu, L. F.; Yan, Y.; Che, R. C.; Chen, M.; Wu, L. M. One-Step Fabrication of Ultrathin Porous Nickel Hydroxide-Manganese Dioxide Hybrid Nanosheets for Supercapacitor Electrodes with Excellent Capacitive Performance. *Adv. Energy Mater.* **2013**, 3 (12), 1636–1646.
- (57) Guan, B. Y.; Kushima, A.; Yu, L.; Li, S.; Li, J.; Lou, X. W. Coordination Polymers Derived General Synthesis of Multishelled Mixed Metal-Oxide Particles for Hybrid Supercapacitors. *Adv. Mater.* **2017**, 29 (17), 1605902.
- (58) Wang, Z. F.; Liu, Y. S.; Gao, C. W.; Jiang, H.; Zhang, J. M. A porous Co(OH)(2) material derived from a MOF template and its superior energy storage performance for supercapacitors. *J. Mater. Chem. A* **2015**, 3 (41), 20658–20663.
- (59) Wang, X.; Yan, C. Y.; Sumboja, A.; Lee, P. S. High performance porous nickel cobalt oxide nanowires for asymmetric supercapacitor. *Nano Energy* **2014**, *3*, 119–126.
- (60) Yu, X. Z.; Lu, B. A.; Xu, Z. Super Long-Life Supercapacitors Based on the Construction of Nanohoneycomb-Like Strongly Coupled CoMoO-3D Graphene Hybrid Electrodes. *Adv. Mater.* **2014**, *26* (7), 1044–1051.
- (61) Kim, S. Y.; Jeong, H. M.; Kwon, J. H.; Ock, I. W.; Suh, W. H.; Stucky, G. D.; Kang, J. K. Nickel oxide encapsulated nitrogen-rich carbon hollow spheres with multiporosity for high-performance pseudocapacitors having extremely robust cycle life. *Energy Environ. Sci.* 2015, 8 (1), 188–194.
- (62) Wang, Y. G.; Song, Y. F.; Xia, Y. Y. Electrochemical capacitors: mechanism, materials, systems, characterization and applications. *Chem. Soc. Rev.* **2016**, 45 (21), 5925–5950.
- (63) Li, B.; Dai, F.; Xiao, Q. F.; Yang, L.; Shen, J. M.; Zhang, C. M.; Cai, M. Nitrogen-doped activated carbon for a high energy hybrid supercapacitor. *Energy Environ. Sci.* **2016**, 9 (1), 102–106.
- (64) Zhao, Y.; Hu, L. F.; Zhao, S. Y.; Wu, L. M. Preparation of MnCo2O4@Ni(OH)(2) Core-Shell Flowers for Asymmetric Supercapacitor Materials with Ultrahigh Specific Capacitance. *Adv. Funct. Mater.* **2016**, 26 (23), 4085–4093.
- (65) Qin, K. Q.; Liu, E. Z.; Li, J. J.; Kang, J. L.; Shi, C. S.; He, C. N.; He, F.; Zhao, N. Q. Free-Standing 3D Nanoporous Duct-Like and Hierarchical Nanoporous Graphene Films for Micron-Level Flexible Solid-State Asymmetric Supercapacitors. *Adv. Energy Mater.* **2016**, 6 (18), 1600755.